ChemSusChem

Research Article
doi.org/10.1002/cssc.202501799

Chemistry Europe
European Chemical Societies Publishing

www.chemsuschem.org

Self-Standing Carbon Nanofibers@Carbon Felt Electrodes to Boost Electrolyzer Productivity: Application to the Electro-Manufacturing of *trans*-3-Hexenedioic Acid and Adipic Acid

Abbas Elhambakhsh, Lun An, Long Qi, and Jean-Philippe Tessonnier*

The industrial implementation of electrosynthesis for chemical manufacturing remains constrained by the limited surface area of conventional electrodes. Herein, this challenge is addressed by designing a carbon nanofiber@carbon felt (CNF@CF) electrode platform that combines the high conductivity, flexibility, and ease of handling of commercial carbon felts (CF) with the large surface area and tunable surface chemistry of carbon nanofibers (CNFs). CNFs are deliberately grown onto the CF scaffold to form a sword-in-sheath structure, where entangled nanofibers wrap the felt macrofibers to provide excellent mechanical stability and electrical conductivity without binders. CNF@CF is evaluated both as an electrode and as a catalyst support for the electrochemical hydrogenation of *cis,cis*-muconic acid (*cc*MA), a biobased platform molecule key to the production of performance polyamides and renewable Nylon 6,6. As a noncatalytic electrode for the partial hydrogenation to *trans*-3-hexenedioic acid, CNF@CF achieves a threefold increase in both cumulative productivity and Faradaic efficiency (FE) compared to bare CF. A similar boost in catalytic activity and energy efficiency is observed using Pd/CNF@CF for the hydrogenation of *cc*MA to adipic acid. These results highlight the opportunities of the CNF@CF platform for electro-organic synthesis and sustainable chemical manufacturing.

1. Introduction

Electrosynthesis is increasingly recognized as a promising approach to decarbonize chemical manufacturing and accelerate the transition to a net-zero economy. In addition to leveraging renewable electricity to drive reactions, electrosynthesis enables the selective conversion of renewable feedstocks, including CO_2, biomass, and fermentation-derived intermediates, in green solvents under near-ambient conditions.[1–3] For oxidation and reduction processes, electrosynthesis also allows for the in situ production of redox reagents, enhancing process safety and minimizing waste.[4,5] Despite these advantages, the industrial adoption of electrosynthesis for chemical manufacturing remains hampered by technical barriers. In particular, scaling up electrolyzers is notoriously difficult as increasing electrode surface area is constrained by mechanical and design limitations.[6–8]

Since electrochemical reactions occur at surfaces, transitioning from conventional flat metal electrodes to three-dimensional materials would increase the total surface area without altering the electrode's geometric area or reactor footprint. Lessons from heterogeneous catalysis underscore the value of nanostructuring materials to enhance specific surface area and improve reaction kinetics while maintaining a constant catalyst mass and volume.[9–11] This strategy has already informed a common approach in fuel cell research, where high-surface-area catalysts are drop-cast onto carbon paper or carbon felt (CF) used as conductive supports.[12–14] However, the polymeric binders required to immobilize the catalyst powders can encapsulate and block active sites, limiting their accessibility. This process also often produces dense catalyst layers that impede mass transport, particularly in liquid-phase reactions or when gaseous byproducts such as H_2 or O_2 are generated through water electrolysis.[15,16]

Here, we developed a binder-free, high-surface-area, hierarchical carbon electrode to boost productivity in electrolyzers. Our design combines the high external surface area, low porosity, and tunable surface chemistry of carbon nanofibers (CNFs) with the macroscopic shape, mechanical strength, high electrical conductivity, and processability of carbon felt. Because physical deposition methods would result in weak interactions between CNFs and the CF scaffold, we adopted a chemical strategy to grow entangled CNFs directly onto the support. This process yields a sword-in-sheath structure in which entangled CNFs wrap

A. Elhambakhsh, J.-P. Tessonnier
Department of Chemical & Biological Engineering
Iowa State University
Ames IA 50011, USA
E-mail: tesso@iastate.edu

A. Elhambakhsh, J.-P. Tessonnier
Center for Biorenewable Chemicals (CBiRC)
Ames IA 50011, USA

L. An, L. Qi
U.S. DOE Ames National Laboratory
Iowa State University
Ames IA 50011, USA

Supporting information for this article is available on the WWW under https://doi.org/10.1002/cssc.202501799

around the macroscopic CF fibers (CNF@CF), providing high surface area and excellent electrical conductivity without requiring a binder. The entangled CNFs also play a role analogous to steel reinforcement in concrete, imparting structural integrity and mechanical stability under liquid flow and gas evolution, with no detachment or loss of nanofibers during electrolysis.

We evaluated CNF@CF both as an inert electrode and as a catalyst support for the electrohydrogenation of *cis,cis*-muconic acid (*cc*MA), a biobased diacid recently elevated to platform molecule status due to its central role in the synthesis of commodity and specialty monomers.[17–19] This reaction was selected for its combined industrial relevance and environmental impact. The noncatalytic electrohydrogenation of *cc*MA yields *trans*-3-hexenedioic acid (*t*3HDA), a novel monomer for high-performance polyamides,[19–23] while the electrocatalytic pathway produces adipic acid (AA), a key precursor for resins, Nylon 6,6, and other industrial chemicals (**Scheme 1**).[17,18,24,25] The global annual production of fossil-based AA was estimated at 3000 kilotonnes in 2020, representing a market value of USD 6.7 billion, with projections reaching USD 8.0 billion by 2024, underscoring its economic and industrial significance.[26,27] The sustainable production of AA is particularly significant, as conventional petroleum-based AA synthesis is the third most polluting manufacturing process after steel and cement, contributing over 3.1 million tons of annual greenhouse gas emissions globally.[28–31]

By tuning the CNFs' degree of entanglement, surface functionalization, and dispersion of the metal active phase, we achieved threefold increase in AA cumulative productivity and a 2.3-fold increase in Faradaic efficiency (FE), substantially enhancing the economic and environmental viability of this pathway. Beyond *cc*MA hydrogenation, the modularity of the CNF@CF platform offers a promising route to design robust, high-performance electrodes for a wide range of electrochemical transformations relevant to sustainable chemical manufacturing, electro-organic synthesis, and energy storage.

2. Results and Discussion

2.1. Synthesis and Structural Design of CNF@CF Electrodes

CNFs were synthesized using a catalyzed chemical vapor deposition (CCVD) method using nickel (Ni) nanoparticles,[32–34] with some modifications to grow CNFs onto the surface of the CF scaffold (**Figure 1**). We deliberately chose to grow CNFs instead of carbon nanotubes (CNTs), although CNTs typically present a higher surface area, to avoid creating internal porosity that could lead to mass transfer limitations during electrochemical reactions. In CNF@CF, the entire surface is external and in direct contact with the electrolyte.

The use of Ni nanoparticles as a catalyst for CNF synthesis offered the advantage of growing nanofibers with uniform shape and size (*vide infra*). More importantly, the low calcination temperature required to decompose the Ni nitrate precursor and form nickel oxide (NiO) nanoparticles prevented any risk of combustion of the CF support. To confirm this, we performed thermogravimetric analysis (TGA) on CF and Ni/CF in air (Figure S1, Supporting Information). The onset temperature for combustion was 625 °C for CF and 425 °C for Ni/CF, indicating that Ni catalyzed the combustion and reduced the onset temperature by 200 °C. It also confirmed that the CF remained intact during the calcination process, which was conducted at 350 °C.

During CNF synthesis, the linear increase in weight with time indicated the absence of any deactivation of the Ni nanoparticles over the course of the reaction (120 min), even though metal encapsulation by carbon is a common deactivation mechanism during CNF and CNT synthesis.[35] This linear trend (Figure S2, Supporting Information) also meant that the nanocarbon loading and overall density of the CNF layer on and around the CF macrofibers could be precisely controlled by adjusting the reaction time. Optical images of the resulting materials revealed no significant change in size, shape, or thickness of the felt between 10 and 60-min growth times, corresponding to CNF loadings relative to the initial CF mass of 60 to 440%, respectively (**Figure 2**a). This suggests that CNFs primarily grew within the voids of the felt, between the macrofibers, increasing the composite's density by a factor of 5.4 without altering the macroscopic morphology of the CF scaffold. However, significant expansion and distortion of the CF were observed at longer reaction times (90 and 120 min), corresponding to CNF loadings of 660% and 770%. Breaking the network of macrofibers at these higher loadings rendered the material more brittle (Figure 2a) and unsuitable for electrochemical operation in a flow reactor. Conversely, a loading of 230% was sufficient to significantly enhance both the surface

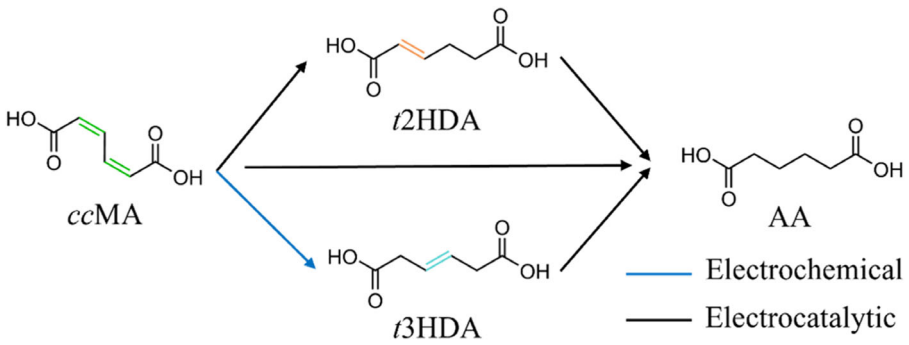

Scheme 1. Proposed chemical reaction pathways for the ECH of *cis,cis*-muconic acid (*cc*MA) to *trans*-2-hexenedioic acid (*t*2HDA), *trans*-3-hexenedioic acid (*t*3HDA), and AA.

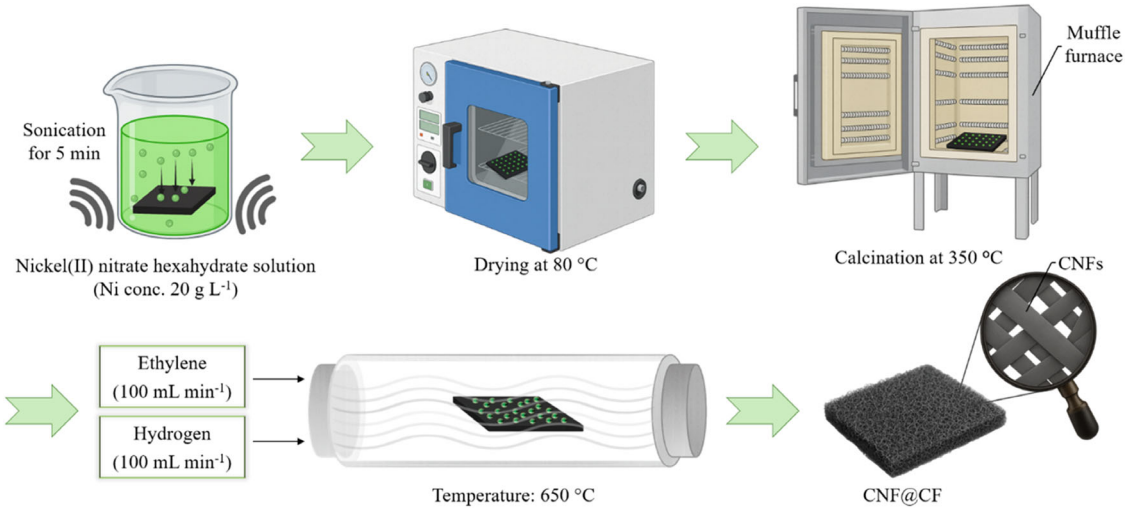

Figure 1. Schematic diagram of CNF@CF synthesis by CCVD.

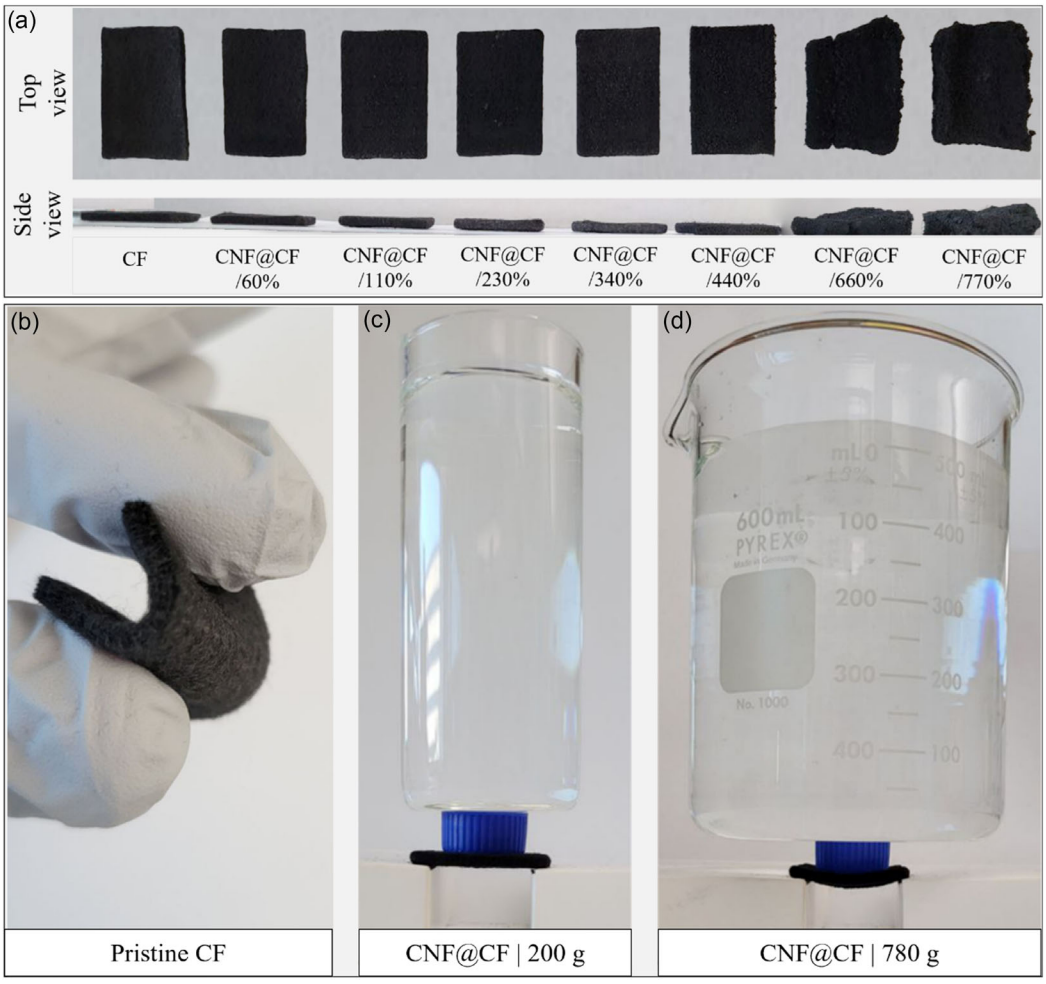

Figure 2. a) Top and side view photographs of the synthesized CNF@CF samples with CNF loadings relative to the initial CF mass of 60, 110, 230, 340, 440, 660, 770%. Photographs of the CNF@CF/660% and CNF@CF/770% samples were captured before the sonication and washing steps. At this stage, the high CNF loadings had significantly altered the CF structure, compromising its mechanical stability. Consequently, during sonication and washing, these samples became fragile, resulting in their collapse into a powder. b) Photograph of the bare CF sample, illustrating its poor mechanical properties. The material lacks sufficient stiffness and can be easily folded with minimal finger pressure. c,d) Mechanical strength test of CNF@CF/230% (30 × 32 mm) using a 2.2 cm-diameter blue spacer. (c) The sample remains fully intact and supports a 200 g load (water and container) without deformation. (d) Even under a significantly higher load of 780 g (beaker with water), the structure only begins to slightly fold, highlighting the mechanical reinforcement compared to bare CF.

area and mechanical properties of the resulting CNF@CF composite. As shown in Figure 2b–d, this material sustained a weight of over 200 g without any deformation, and only slight deformation began to occur when a weight of 780 g was applied.

2.2. Structural and Morphological Characterization of CNF@CF

Field-emission scanning electron microscopy (FE-SEM) images revealed that CNFs were grown directly on the CF scaffold, resulting in the formation of entangled nanostructures anchored to the felt fibers. This hierarchical architecture enabled a binder-free integration of nanostructured carbon onto a robust, conductive macroscopic framework. **Figure 3** presents a series of FE-SEM images comparing the morphology of bare CF and the CNF@CF sample with a loading of 230% at different magnifications. While bare CF exhibits relatively smooth surfaces with large voids between the fibers, the CNF@CF sample reveals complete and homogeneous coverage of the felt fibers by randomly entangled CNFs. This sword-in-sheath structure forms a dense but porous layer that increases the overall surface area and mechanical robustness of the electrode. Image analysis revealed an average diameter for the CF macrofibers of 17 μm. After synthesis, the diameter of the CNF@CF fibers increased to 41 μm,

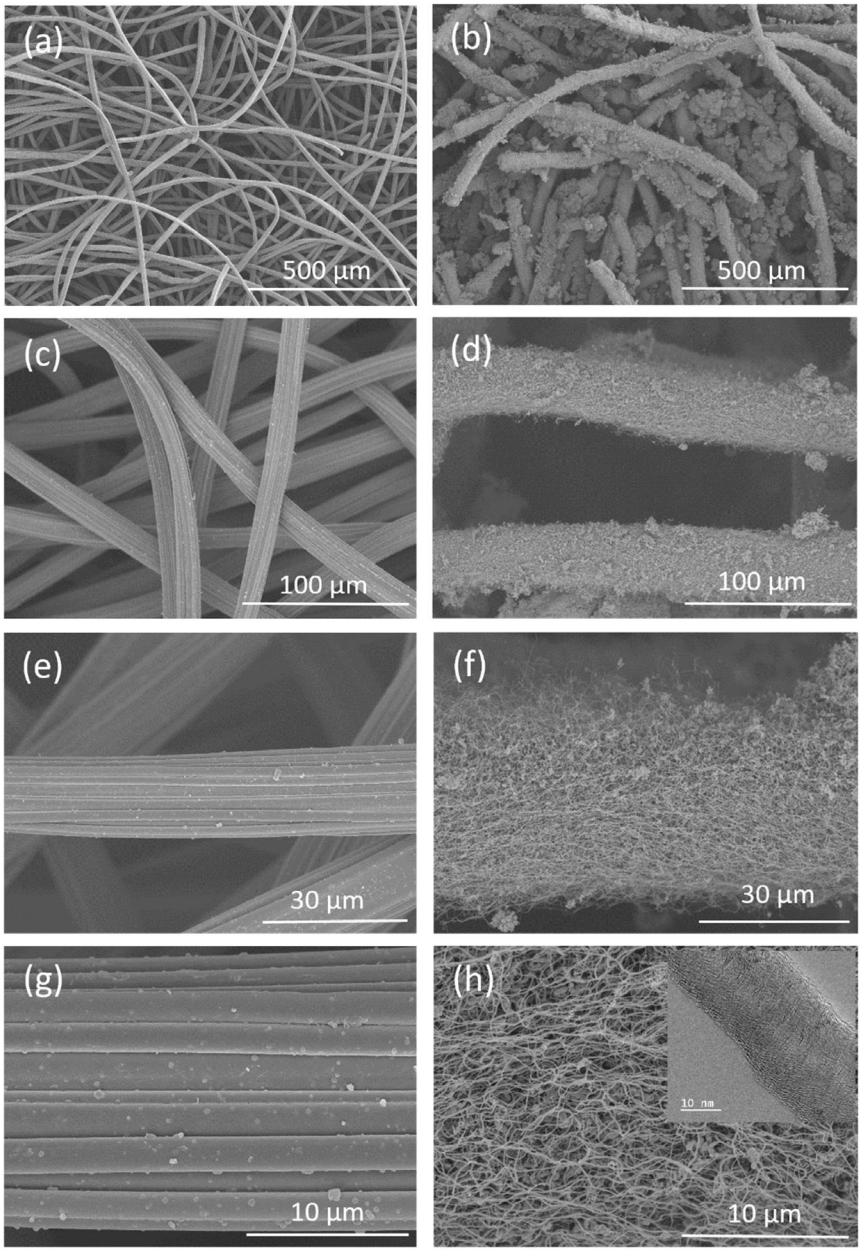

Figure 3. FE-SEM images of CF a,c,e,g) and CNF@CF b,d,f,h) with a CNF to CF ratio of 230%. The images were taken at different magnifications, showing complete and homogeneous coverage of the CF surfaces with CNFs. Insert: TEM image showing the microstructure of a CNF.

indicating the formation of a dense CNF layer with a thickness of 12 μm entangled around the CF macrofibers.

Transmission electron microscopy (TEM) analysis further confirmed the successful synthesis of CNFs on the CF support. As shown in Figures S3,S4, Supporting Information, the CNFs appear as straight to slightly curved filaments with an average CNF diameter of 19.7 nm. Low-magnification images also show contrast suggestive of an inner channel similar to carbon nanotubes (Figure S3a–e, Supporting Information). However, higher-magnification images reveal inner walls that seal off the channel, rendering the inner volume inaccessible (Figures S3f,g, Supporting Information).

Surface area measurements using nitrogen physisorption were consistent with optical and FE-SEM observations, showing a correlation between CNF growth time and the surface area of the resulting CNF@CF composite. While the pristine CF scaffold exhibited a negligible specific surface area of ≈1 $m^2 g^{-1}$, it increased to 35 $m^2 g^{-1}$ after only 10 min of CNF growth (CNF@CF/60%). The surface area further increased to 90 $m^2 g^{-1}$ for CNF@CF/230% (**Figure 4**a) but then plateaued and slightly decreased for CNF@CF/340% and CNF@CF/440% (**Table 1**). This decline is attributed to the formation of a dense CNF network and partial surface coverage by overlapping filaments, ultimately leading to the structural expansion and distortion observed at CNF loadings of 660% and 770%. Barrett–Joyner–Halenda analysis of the pore size distribution further confirmed that the samples are mesoporous with an average pore size of 11.6 nm for CNF@CF/230% (Insert in Figure 4a).

2.3. Surface Chemistry and Graphitic Character of CNF@CF

Raman spectroscopy and X-ray photoelectron spectroscopy (XPS) were employed to evaluate the structural order and surface chemistry of the CNF@CF samples. The Raman spectra (Figure 4b, S5–S6, Supporting Information Table 1) displayed prominent D1 and G bands, corresponding to structural defects and graphitic domains, respectively. The area ratio of these bands (I_G/I_D) decreased systematically with increasing CNF loading, from 1.65 to 0.78 for CNF@CF/230%, indicating that the CNFs are significantly more defective than the underlying graphitic CF scaffold. As the CNF layer surrounding the CF macrofibers thickened, the I_G/I_D ratio stabilized in the range of 0.7–0.8. This observation is consistent with the 12 μm thick CNF layer observed by FE-SEM that homogeneously wraps the CF fibers and prevents the laser light from penetrating the sample (Table 1). This also suggests that the CF surface was nearly fully covered with CNFs at a loading of 230%. Beyond this point, Raman analysis primarily probed the uppermost CNF layers, and further CNF growth did not substantially affect the observed graphitic character.

The C 1s peak in the XPS spectra provided additional insights into the carbon bonding environment in the CF and CNF@CF samples (Figure 4c,S7, Supporting Information and Table 1). For graphitic carbon, the main peak typically appears near 284.5 eV, corresponding to aromatic sp^2-hybridized carbon.[36,37] Secondary peaks at slightly higher binding energies indicate sp^3-hybridized carbon (≈285 eV) commonly associated with structural defects or amorphous regions, as well as oxygen-containing functional groups such as C–O, C═O, and O–C═O (≈286–289 eV). The intensity ratio of the sp^2 to sp^3 peaks serves as an indicator of graphitization, with a higher ratio reflecting a more graphitic structure. As shown, the sp^2/sp^3 ratio decreased from 3.88 for the pristine CF to 2.69 for CNF@CF/60, consistent with the trend observed in the Raman analysis. This ratio remained nearly constant across CNF loadings from 110% to 440%, likely due to the limited probing depth of XPS, which typically samples only the

Table 1. Effect of CNF loading (60%–440%) on the surface area, I_G/I_D ratio from Raman spectra, and sp^2/sp^3 ratio from C 1s XPS analysis of CNF@CF samples.

Sample	Surface area [BET, $m^2 g^{-1}$]	I_G/I_D	sp^2/sp^3 ratio
Bare CF	≈1	1.65	3.88
CNF@CF/60%	35	1.04	2.69
CNF@CF/110%	67	0.77	2.50
CNF@CF/230%	90	0.78	2.58
CNF@CF/340%	84	0.72	2.28
CNF@CF/440%	83	0.68	2.35

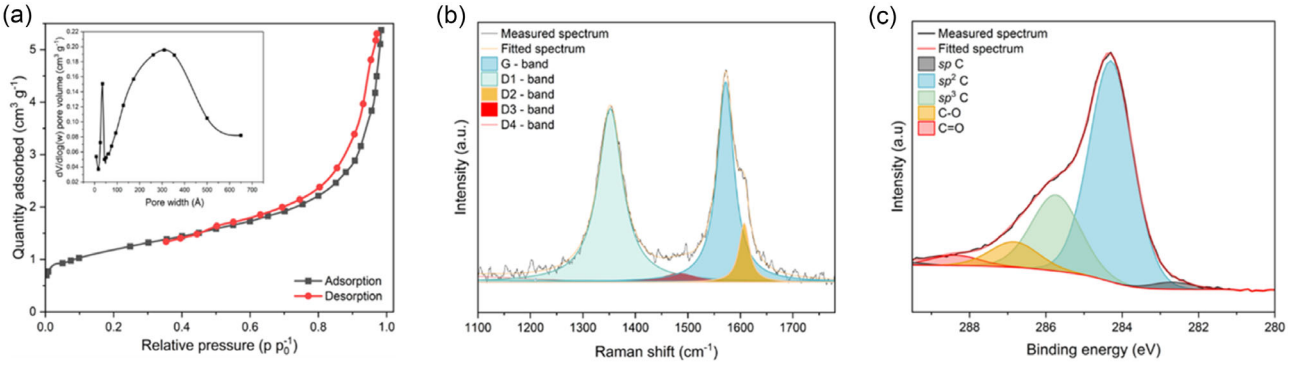

Figure 4. Textural, structural, and chemical characterization of CNF@CF/230%. a) N_2 adsorption–desorption isotherm and pore size distribution (insert), revealing a mesoporous structure with a surface area of 90 $m^2 g^{-1}$. b) Raman spectrum showing G and D1–D4 bands, revealing graphitic and defect-related features. c) C 1s XPS peak deconvolution indicating a sp^2/sp^3 ratio of 2.58.

top 5–10 nm of the material surface. As a result, XPS primarily probed the outermost CNF layers, which exhibit similar structural features regardless of growth time and overall CNF loading.

2.4. Influence of Oxygen Functional Groups

To enhance the hydrophilicity of CNF@CF electrodes and evaluate the effect of surface chemistry on their electrochemical performance, representative CF and CNF@CF/230% samples were oxidized in nitric acid and thermally annealed at selected temperatures up to 800 °C to tune the concentration of surface oxygen-containing groups. XPS analysis (Table S1, Supporting Information) revealed a higher oxygen content in oxidized CNF@CF compared to CF (13.1 at% vs 8.0 at%, respectively). The oxygen-containing groups were also more stable on CNF@CF, with 6.7 at% remaining after annealing at 800 °C versus only 3.3 at% for CF. This difference is attributed to the higher defect density in the CNF structure, which provides more sites for thermally stable moieties such as lactones, phenols, and ether groups.

Raman spectroscopy supported this observation, showing a modest but consistent increase in the I_G/I_D ratio for CNF@CF samples with increasing annealing temperature (Figure S6, Table S2, Supporting Information). The ratio increased from 0.49 for the unannealed oxidized sample to 0.64 after annealing at 800 °C, suggesting mild restructuring or partial healing of defects during thermal treatment. These findings highlight the superior capacity of CNF-rich surfaces to incorporate and retain thermally stable oxygen functionalities, which can improve wettability, enhance mass transport, and support catalytic activity in aqueous electrosynthetic systems.

2.5. Impact of CNFs on *cc*MA Hydrogenation Performance

The performance of the CNF@CF composites and the influence of CNF growth were evaluated for the electrochemical hydrogenation (ECH) of *cc*MA to *t*3HDA, used here as a model reaction representative of a broad class of noncatalytic electro-organic transformations.[38] Prior kinetic studies, isotopic labeling, electron paramagnetic resonance (EPR) spectroscopy, and theoretical calculations have shown that this reaction proceeds via outer-sphere electron and proton transfer in solution, across a wide range of early, late, and post-transition metal electrodes.[17,18,24,25] For carbon-based electrodes, activity differences are therefore attributed to variations in surface defects and oxygen-containing functionalities, which modulate the charge transfer resistance at the solid-liquid interface, rather than to any intrinsic catalytic effect of the carbon surface itself.

The samples were evaluated using linear sweep voltammetry (LSV) in a conventional electrochemical cell, while chronoamperometry (CA) was performed in a MicroFlow cell (Figure S8, Supporting Information). All experiments were performed using a sodium phosphate buffer at pH 7 to prevent the pH-driven isomerization and lactonization of *cc*MA,[39] enhance the solubility of organic reactants and products,[40] and maintain a stable reaction environment throughout the duration of the bulk electrolysis experiments. LSV measurements in blank electrolyte (0.2 M sodium phosphate buffer, pH ≈ 7.0) revealed the onset of hydrogen evolution reaction (HER) at −1.60 V versus Ag/AgCl for both CF and CNF@CF/230% (**Figure 5**). In the presence of *cc*MA, the onsets shifted to −1.42 V and −1.31 V for CF and CNF@CF/230%, respectively. The 110 mV difference reflects the contribution of ECH and improved surface interactions with *cc*MA in solution due to CNFs' surface chemistry, which favors ECH over HER. While both reactions co-exist, CNFs selectively promote ECH, leading to substantial gains in productivity and FE (*vide infra*).

As Ni nanoparticles were used as catalysts for CNF growth, control experiments were performed to assess whether residual Ni could influence the electrochemical performance of the CNF@CF composites. CNF@CF/230% electrodes were treated with 2 M HCl at 80 °C for 2 h to remove residual Ni species. This acid treatment resulted in a ≈4.9% weight loss, attributed to both Ni dissolution and the detachment of loosely anchored CNFs. Inductively coupled plasma optical emission spectroscopy (ICP-OES) analysis confirmed the complete removal of Ni following acid washing (Table S3, Supporting Information). To reproduce the thermal history of the pristine sample and eliminate any surface functionalities introduced during the acid treatment, the electrodes were subsequently annealed at 650 °C under inert atmosphere. The ECH of *cc*MA was then evaluated at −1.5 V versus Ag/AgCl using the acid-washed electrodes. As shown in Figure S9, Supporting Information, the conversion and FE were unchanged within experimental error compared to the untreated sample. These results indicate that residual Ni contributes at most ≈5.6% to the observed activity, thereby justifying the decision not to subject the other CNF@CF samples to further purification.

The effect of CNF loading on hydrogenation performance was further assessed by CA at −1.5 V versus Ag/AgCl over 90 min (**Figure 6**a,b, S10, Supporting Information). Compared to bare CF (18.8% conversion, 0.76 g L^{-1} cumulative productivity of *t*3HDA), CNF@CF/60% has more than doubled both metrics (46.2%,

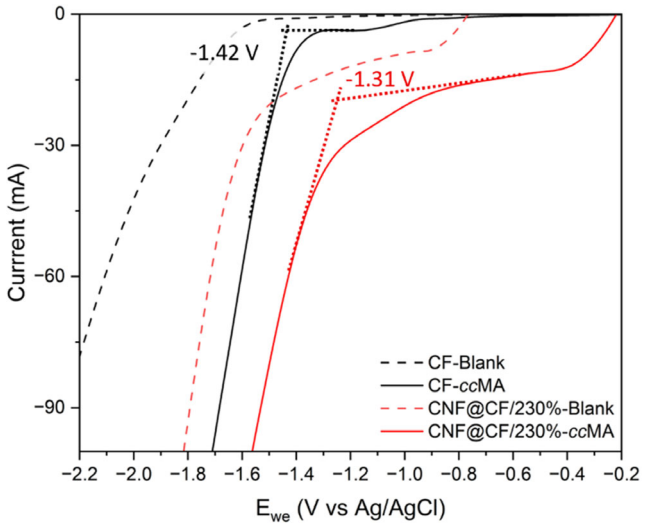

Figure 5. LSV curves for CF and CNF@CF/230% electrodes in 0.2 M sodium phosphate buffer (pH ≈ 7.0), with and without 5.0 g L^{-1} of *cc*MA.

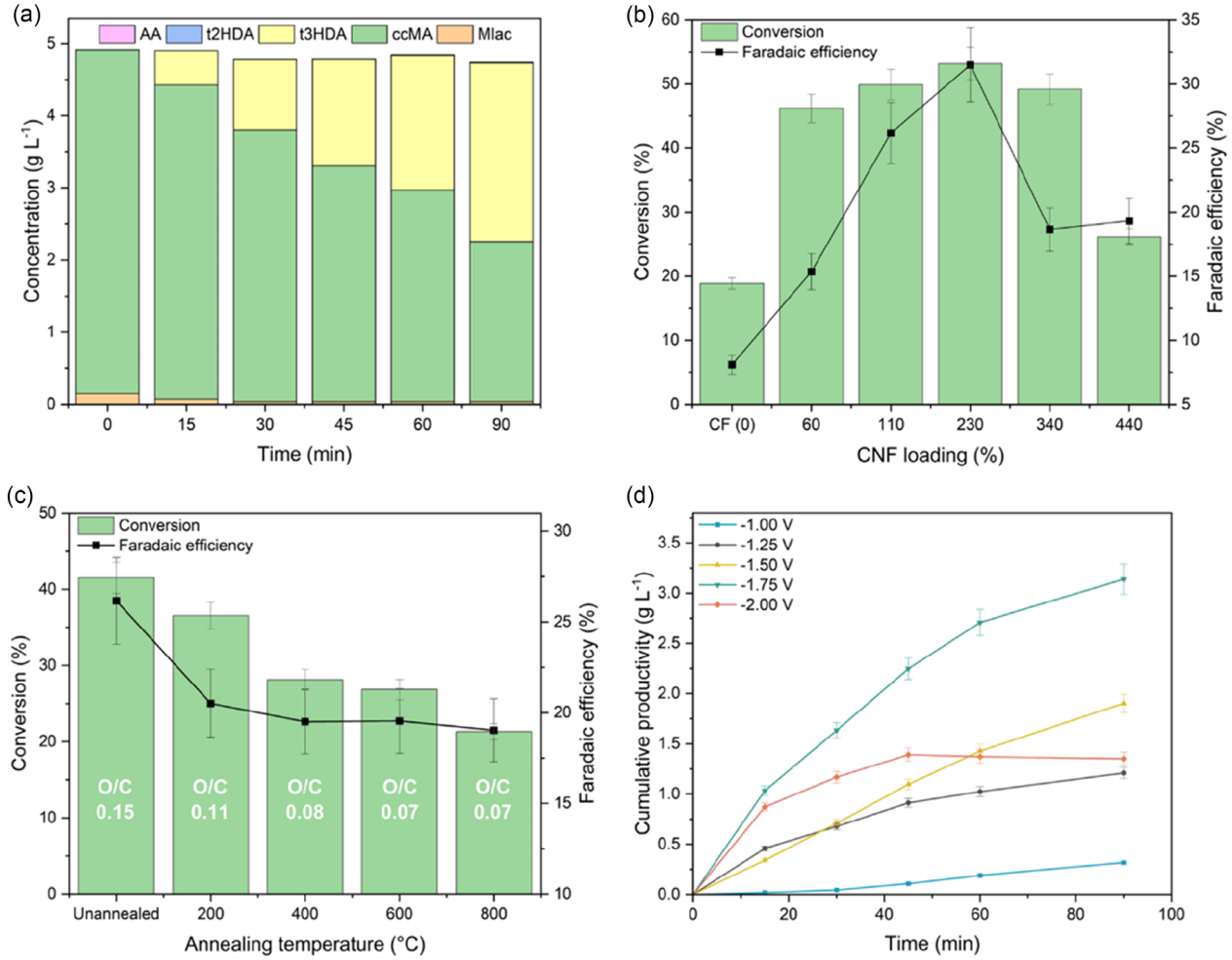

Figure 6. a) Concentration profile of *cc*MA and its hydrogenation products over 90 min reaction at −1.5 V versus Ag/AgCl using the CNF@CF/230% electrode. b) Summary of *cc*MA conversion and FE for CF and CNF@CF electrodes with CNF loadings ranging from 60% to 440% at the end of the 90-min reaction. c) FE and *cc*MA conversion after 90-min reaction for oxidized CNF@CF/230% electrodes annealed at different temperatures; higher oxygen contents, expressed as O/C atomic ratios determined by XPS, correlate with improved conversion and FE. d) Impact of applied potential on *cc*MA hydrogenation using oxidized CNF@CF/230% electrodes. Reactions were performed at −1.00, −1.25, −1.50, −1.75, and −2.00 V versus Ag/AgCl in 0.2 M sodium phosphate buffer containing 5 g L^{-1} *cc*MA. While performance improved with increasing potential up to −1.75 V, the electrode showed complete deactivation at −2.0 V, likely due to HER-induced surface blocking and changes in surface functionalization.

1.82 g L^{-1}). Higher CNF loading further improved the electrode's performance: CNF@CF/110% and CNF@CF/230% yielded conversions of 49.8% and 53.2%, with corresponding productivities of 2.23 g L^{-1} and 2.35 g L^{-1}, respectively. Notably, CNF@CF/230% shows a threefold enhancement in terms of cumulative productivity. Besides, FE also improved substantially by fourfold, from 8.0% for CF to 31.4% for CNF@CF/230%. These enhancements are attributed to the larger specific surface area (Table 1), which increases the effective contact area with the electrolyte and may enhance local fluid dynamics near the electrode, reducing mass transfer limitations. The lower graphitic character of CNF@CF relative to CF, evident from Raman and XPS analyses (Figure 4 and S5, Supporting Information Table 1), may further improve wettability and facilitate access of the aqueous phase to the electrode's 3-dimensional pore network.

However, at higher CNF loadings (340% and 440%), both conversion and FE declined significantly, likely due to excessive filament overlap that blocks inter-thread porosity and impedes electrolyte penetration into the CF matrix. These diffusion barriers may be exacerbated by the local trapping of hydrogen bubbles from concurrent HER, which further limits access to internal electrode surfaces. Together, these findings underscore the importance of optimizing CNF coverage to balance surface area, porosity, and electrochemical accessibility in hierarchical electrode design.

As the acid treatment with HCl led to a ≈4.9% weight loss, the long-term mechanical stability of CNF@CF/230% under reaction conditions was further investigated by recycling the same electrode for five consecutive 90-min CA experiments at −1.50 V versus Ag/AgCl (Figure S11, Supporting Information). The reactor system was thoroughly rinsed between each run by flowing 100 mL of fresh *cc*MA solution to remove any residual reactants and products. The rinsing solution was then purged from the reactor and tubing by flowing air for 15 min, and a new batch

of 100 mL *cc*MA solution was connected for the next run. The conversions measured at the end of each 90-min experiment showed a modest decline (≈12% drop) during the first two experiments, after which their performance stabilized at ≈40% for subsequent runs. The recovered solutions were then combined and filtered using a polyethersulfone (PES) membrane (0.8 μm, 47 mm, Sterlitech) to recover and quantify any detached CNFs. ≈2.3 mg of CNFs were recovered, representing a cumulative weight loss of only ≈0.56%, confirming that the CNF@CF electrode maintained a stable structure throughout the five experiments (450 min total reaction time). This suggests that the change in reaction rate over the first two cycles is likely due to alterations to the electrode's surface structure or chemistry driven by the applied potential and/or species in solution. However, once the CNF@CF electrodes reach a thermodynamically stable state, they retain their activity after repeated use, indicating that they are durable and not limited to single-use applications.

2.6. Impact of Oxygen Functional Groups on CNF@CF Electrode Performance

To investigate the role of oxygen-containing functional groups on ECH activity, CNF@CF/230% electrodes were oxidized with nitric acid and annealed at various temperatures (25 °C to 800 °C) to tune the surface oxygen content. It is to be noted that the oxidative treatment was performed under mild conditions known to introduce oxygen functionalities without altering the structural and textural properties of carbon materials. N_2 physisorption confirmed it, as the CNF@CF/230% sample exhibited identical surface areas before and after oxidation (90 vs 89 m^2 g^{-1}). Therefore, activity trends for these samples can be directly correlated to surface oxygen content determined by XPS (Table S1, Supporting Information).

Chronoamperometric hydrogenation of *cc*MA at −1.5 V versus Ag/AgCl (Figure 6c, S12,13, Supporting Information) revealed a linear correlation between oxygen content and ECH performance (Figure S13, Supporting Information). The unannealed CNF@CF/230% electrode, with the highest oxygen loading (13.1 at%), achieved the best results: 41.5% conversion and 26.4% FE. As the oxygen content decreased with thermal annealing, conversion and FE declined accordingly. The sample annealed at 800 °C, retaining only 6.7 at% oxygen, showed the lowest performance, with 26.8% conversion, and 18.5% FE.

To further probe the influence of electrochemical driving force, ECH experiments were conducted at different applied potentials using the oxidized CNF@CF/230% sample (Figure 6d, S14, Supporting Information). Increasing the potential from −1.0 to −1.75 V versus Ag/AgCl led to continuous improvements in conversion and FE, consistent with enhanced electron transfer kinetics. However, a sharp decline in performance was observed at −2.0 V. After 45 min, the electrode became inactive for ECH, with no further conversion detected during the remaining reaction time. The FE dropped below 6%, indicating that HER became the dominant electrochemical process.

The origin of this deactivation was investigated by XPS, comparing the C 1s and O 1s spectra of oxidized CNF@CF/230% electrodes before reaction and after 90 min of electrolysis at −1.5 V and −2.0 V versus Ag/AgCl (Table S4, Supporting Information). In the absence of *cc*MA (blank electrolyte), the electrode tested at −1.5 V versus Ag/AgCl retained its surface oxygen-containing functional groups, with the oxygen concentration decreasing only slightly from 13.1 at% (O/C ≈ 0.15) to 12.3 at%, well within the XPS measurement error. Similarly, the oxygen concentration increased only slightly to 14.1 at% (O/C ≈ 0.16) when the reaction was performed in the presence of *cc*MA, indicating that the electrode surface remains chemically stable under those conditions. In contrast, at −2.0 V in blank electrolyte, the oxygen content dropped sharply to 6.1 at%, consistent with the stronger reducing conditions. However, when *cc*MA was present, the surface oxygen level increased dramatically to 21.1 at%, indicating significant surface fouling by organic species. Although a detailed investigation would be necessary to elucidate the fouling mechanism, one plausible explanation is that organic radicals generated via sequential electron–proton transfer (previously detected by EPR) may react with surface defects and form covalent bonds, following a mechanism analogous to the radical-induced grafting process reported by Zhang et al.[41]

Together, these results underscore the importance of surface oxygen groups in improving wettability and facilitating proton-coupled electron transfer. They also highlight that both surface functionalization and applied potential must be co-optimized to ensure sustained and efficient operation.

2.7. Modularity of CNF@CF Electrodes for Electrocatalysis as Binder-Free Supports

Beyond their role as hydrogenation electrodes, CNF@CF materials offer a modular platform for electrocatalytic applications. To demonstrate this, we evaluated the CNF@CF/230% sample as a binder-free support for the complete hydrogenation of *cc*MA to AA, using palladium nanoparticles as the active catalyst phase. High-surface-area carbon materials are widely used as supports for metal catalysts in heterogeneous catalysis and electrocatalysis,[14,42] but they are typically employed as powders and require drop-casting with polymeric binders to secure them within electrochemical systems. This approach often blocks active metal sites, induces catalyst detachment, and leads to degradation during operation.[43–45] In contrast, CNF@CF offers a high-surface-area, freestanding architecture that enables direct deposition of metal nanoparticles without binders or additional carbon scaffolds. Electrocatalytic hydrogenation experiments were conducted at −0.7 V versus Ag/AgCl for 360 min, consistent with prior work using a commercial Pd/carbon catalyst,[18] following the procedure described in the experimental section (**Figure 7**). The Pd/CNF@CF catalyst achieved complete hydrogenation of *cc*MA to AA within the reaction time, delivering more than a threefold increase in cumulative productivity compared to Pd/CF. This enhancement was consistent with the higher metal loading on CNF@CF (1.02 mg) compared to CF (0.35 mg), while maintaining similar average particle sizes (Figure S15,16,

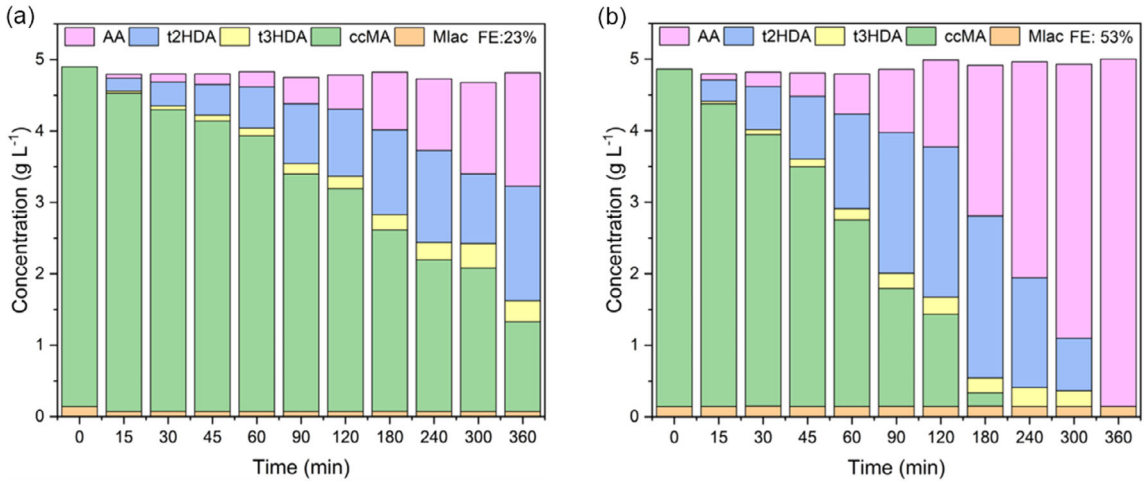

Figure 7. Concentration profiles of *cc*MA and its hydrogenation products during a 360-min reaction at –0.7 V versus Ag/AgCl for a) Pd/CF and b) Pd/CNF@CF. The Pd/CNF@CF system achieved complete conversion to AA with significantly higher FE and cumulative productivity.

Supporting Information). This improvement in metal dispersion was enabled by the significantly higher specific surface area of CNF@CF relative to CF (90 m^2 g^{-1} vs 1 m^2 g^{-1}). Importantly, the FE improved significantly, from 23% for Pd/CF to 52% for Pd/CNF@CF, further suggesting that the carbon nanofibers enhance mass transfer of muconic acid and thereby favor electrocatalytic hydrogenation over hydrogen evolution. These results illustrate the opportunities of CNF@CF materials as tunable, binder-free supports for electrocatalysis.

3. Conclusion

This study demonstrates a simple yet versatile approach for engineering hierarchical carbon electrodes with high surface area and tunable surface chemistry, enabling efficient ECH of *cis,cis*-muconic acid to *trans*-3-hexenedioic acid in aqueous media. CNFs grown directly on carbon felt significantly enhanced hydrogenation performance by increasing electrochemically active surface area and reducing graphitic character. The defective structure of CNFs served as effective anchoring sites for oxygen-containing functional groups, which remained stable even at high annealing temperatures, crucial for preparing hydrophilic electrodes suitable for proton-coupled electrochemical reactions. Furthermore, the ability to control CNF loading and surface oxygen content enabled optimization of both conversion and FE, while highlighting the need to avoid overgrowth and excessive reduction potentials that compromise performance. The modular architecture of CNF@CF electrodes also enables their use as binder-free supports for metal nanoparticles. As demonstrated with Pd, this integration enhanced catalytic activity and selectivity for full *cc*MA hydrogenation to AA.

Together, these results establish CNF@CF as a multifunctional platform for electrosynthesis and heterogeneous catalysis. As the CF scaffold already finds applications in various electrochemical systems, including membrane electrode assemblies, and CNF@CF retains the dimensions and structure of the pristine CF, the synthesized materials can be readily adapted to diverse applications and reactor configurations. As such, this strategy not only advances the electrochemical valorization of biobased intermediates such as *cc*MA, but also opens new avenues for developing tailored carbon supports for a broad range of electrochemical and electrocatalytic transformations.

4. Experimental Section

Materials and Chemicals

cis,cis-Muconic acid (*cc*MA, ≥97.0%), palladium(II) chloride (≥99.9%), sulfuric acid (99.99%), deuterium oxide (D_2O, 99.9 atom% D), and dimethylmalonic acid (DMA, TraceCERT grade for qNMR) were purchased from Millipore Sigma. Nickel(II) nitrate hexahydrate (99.9%, metals basis), nitric acid (67%–70%), sodium phosphate dibasic anhydrous (≥99%), sodium phosphate monobasic monohydrate (>98 %), potassium sulfate (>98%), ethanol (>99.2%), and graphitic carbon felt (CF, 250 × 250 × 3.18 mm, 99.0%) were purchased from Fisher Scientific. Ultra-high purity ethylene (C_2H_4, >99.99%), nitrogen (N_2, >99.99%), and hydrogen (H_2, >99.99%) were supplied by Airgas. Deionized (DI) water (18.2 MΩ·cm, Barnstead E-Pure) was used in all experiments.

Synthesis of CNF@CF Electrodes

Rectangular pieces of graphitic carbon felt (≈30 × 15 × 3.18 mm) were oxidized in concentrated nitric acid (37%) at room temperature for 24 h to create surface oxygen functionalities and improve the interactions between Ni nanoparticles, used here as a catalyst to grow CNFs, and the CF's carbon surface. The oxidized felts were rinsed three times with deionized water and ethanol, then dried overnight at 80 °C. Each oxidized CF piece was subsequently impregnated with an ethanolic solution containing the nickel precursor (99 g L^{-1} nickel(II) nitrate hexahydrate in ethanol) and sonicated for 5 min to displace trapped air and ensure a uniform wetting of the carbon fiber network. After impregnation, the felts were dried in an oven at 80 °C for 24 h, followed by an additional 24 h at 120 °C to remove residual solvent. The resulting Ni/CF samples were calcined in air at 350 °C

(ramp rate: 10 °C min^{-1}) to decompose the nitrate and form NiO nanoparticles. CNFs were grown on the NiO/CF substrates in a horizontal tube furnace (Lindberg/Blue M) equipped with a quartz tube (inner diameter 5 cm, length 90 cm). Each NiO/CF sample was placed in a quartz boat, which was then inserted into the center of the quartz tube and positioned approximately at the midpoint of the heated zone inside the furnace. The system was purged with N_2 (100 mL min^{-1}) at room temperature for 30 min to remove residual air. The furnace temperature was then ramped to 350 °C under N_2, after which the gas flow was switched to H_2 (100 mL min^{-1}) for 30 min to reduce NiO to metallic Ni. Following reduction, the temperature was increased to 650 °C at a ramping rate of 10 °C min^{-1} under H_2. The gas flow was then switched to a 1:1 mixture of C_2H_4 and H_2 with a total flow rate of 200 mL min^{-1} to initiate CNF growth via CCVD.[46] The reaction was stopped at varying times (10, 20, 30, 45, 60, 90, and 120 min) by switching the gas flow to N_2 and turning off the heating, to obtain CNF@CF samples with different CNF loadings. At these time points, CNF@CF samples were obtained with loadings (CNF weight relative to the weight of the initial CF scaffold) of 60%, 110%, 230%, 340%, 440%, 660%, and 770%, respectively. After each sample had fully cooled, it was recovered, sonicated in ethanol for 15 min to remove loosely bound CNFs, rinsed with water and ethanol, and dried at 80 °C for 6 h.

Preparation of Oxidized Electrodes

To investigate the influence of oxygen-containing functional groups and surface polarity on electrode performance, CF and CNF@CF with a loading of 230% (CNF@CF/230%) were immersed in 200 mL of 37% HNO_3 and kept at room temperature for 24 h. The samples were then washed thoroughly with DI water, followed by drying at 80 °C in ambient air for 6 h. The oxidized materials were subsequently annealed in a tube furnace under N_2 flow (100 mL min^{-1}). Samples were heated at a ramp rate of 1 °C min^{-1} to the target temperatures of 25 (unannealed), 200, 400, 600, or 800 °C, and held for 2 h.

TGA

The thermal stability of Ni/CF was evaluated using TGA (Netzsch STA449 F1). ≈5–10 mg of sample was placed in an alumina crucible and heated from room temperature to 1100 °C at a constant rate of 10 °C min^{-1} under a synthetic air atmosphere.

FE-SEM

FE-SEM was used to visualize the CNF coverage on the surface of the CF scaffold. A CNF@CF sample previously sonicated for 30 min in ethanol was imaged using a Hitachi SU4800 field-emission SEM. The extended sonication step helped verify that the nanofibers remained well anchored to the carbon felt, confirming the mechanical robustness of the CNF layer under conditions relevant to electrochemical operation.

TEM

CNF size and microstructure were analyzed by TEM. Although the CNFs were strongly anchored on the CF scaffold, sonicating CNF@CF for 30 min in ethanol detached a minute amount of CNFs sufficient for TEM analysis. A 10 μL aliquot of the obtained solution was dropped onto a holey carbon-coated TEM grid and allowed to dry before analysis with a JEOL 2100 STEM operated at 200 kV.

Nitrogen Physisorption

Surface area of the samples was evaluated through nitrogen adsorption–desorption isotherms at 77 K using a Micromeritics ASAP 2020 analyzer. Prior to measurements, samples were degassed under dynamic vacuum by gradually heating from 25 °C to 200 °C at 5 °C min^{-1}, then maintained at 200 °C for 12 h to remove adsorbed species. The specific surface area was determined using the (New Jersey, USA) Brunauer–Emmett–Teller (BET) method.

Elemental Analysis

ICP-OES (Agilent 5800) was used to quantify bulk nickel and palladium contents. For sample preparation, a known amount of CNF@CF or Pd/carbon catalyst was weighed into a 20 mL scintillation vial and pyrolyzed in air at 550 °C for 170 h in a furnace to burn off the carbon support. After cooling, 6 mL of freshly prepared aqua regia (3:1 HCl:HNO_3) was added to the residue, and the mixture was heated at 80 °C for 5 h to ensure complete dissolution of palladium. The vial was not sealed during digestion to prevent over-pressurization from evolving gases. Once cooled to room temperature, the solution was diluted with 2% HNO_3 and prepared for analysis. Calibration standards containing 0.0, 0.5, 1.0, and 3.0 ppm of Ni or Pd in 2% HNO_3 were used to construct standard curves for quantification.

XPS

XPS analysis was conducted using a Kratos Amicus 3400 spectrometer. CNF@CF samples were analyzed using 240 W unmonochromated Mg Kα X-rays, and photoelectrons emitted at 0° from the surface normal were energy analyzed using a DuPont type analyzer, with the pass energy of 150 eV. Raw data files were processed using CasaXPS, with all spectra energy-calibrated to the sp^2 carbon component at 284.5 eV.[47–49]

Raman Spectroscopy

Raman spectroscopy was used to assess the structural order of the carbon materials. Spectra were acquired using a Renishaw inVia Raman microscope equipped with a 488 nm argon-ion laser (25 mW) and a spectral resolution of 2.0 cm^{-1}. A 50X objective lens was used to focus the laser on the sample, and each spectrum was collected with an acquisition time of 50 s. The analysis was performed over the 1100–1800 cm^{-1} range. Spectral deconvolution followed the method of Knauer et al,[50] using a multicomponent baseline subtraction and peak fitting routine: the G (1580 cm^{-1}), D1 (1350 cm^{-1}), D2 (1620 cm^{-1}), and D4 (1200 cm^{-1}) bands were fitted with Lorentzian functions, and the D3 (1500 cm^{-1}) band with a Gaussian function. Only the D1 and G bands were used to estimate the degree of graphitization, as they correspond to disordered carbon atoms and the in-plane stretching of sp^2-hybridized C═C bonds, respectively. The remaining peaks were excluded from the calculation due to their association with amorphous or nongraphitic domains.

Pd/CF and Pd/CNF@CF Catalysts Synthesis

Catalysts were prepared by electrodeposition of palladium (Pd) on CF and CNF@CF/230%. The deposition was performed using a 100 mL aqueous sulfuric acid solution (1 M) containing 50 mg of palladium chloride salt (30 mg Pd). The electrodeposition was carried out using the cyclic voltammetry (CV) technique for 100 cycles (scan rate:

100 mV s^{-1}) within a potential range of 0 to −0.3 V versus Ag/AgCl. According to ICP measurements, the Pd loadings for a 30 × 15 mm piece of CF and CNF@CF were 0.35 mg and 1.02 mg, respectively, demonstrating an almost threefold increase in the capacity of CNF@CF samples to load Pd nanoparticles compared to bare CF. TEM analysis further revealed that the average diameter of the deposited Pd nanoparticles on CF and CNF@CF supports were 9.07 and 9.32 nm (Figure S15,16, Supporting Information).

ECH of Muconic Acid

ECH experiments were conducted in a Micro Flow Cell reactor (ElectroCell, Amherst, NY) operated in batch mode with external liquid recirculation. The electrolyte consisted of 100 mL of 5 g L^{-1} *cc*MA dissolved in 0.2 M sodium phosphate buffer (pH ≈ 7), stirred at 30 °C for 15 min prior to electrolysis to ensure dissolution and minimize isomerization and cyclization to muconolactone (Mlac).[39] Minor Mlac formation, when detected, was excluded from product quantification, although it is shown in the concentration profile figures. The electrochemical cell employed CNF@CF or bare CF immobilized on a graphite plate (used as a current collector) as the working electrode, platinized titanium as the counter electrode, and a leak-free Ag/AgCl reference electrode mounted at mid-gap using a PTFE separator. Electrodes were spaced 4 mm apart. Electrolyte circulation (180 mL min^{-1}) was maintained using a peristaltic pump (Fisherbrand GP1000). Samples (600 μL) were withdrawn at 15 min intervals up to 90 min, air-dried for 12 h, then reconstituted in D_2O with DMA internal standard. After sonication (8 min), the samples were analyzed by ^{1}H NMR using a Bruker Avance III 600 MHz spectrometer to quantify *cc*MA and its hydrogenated products. All FEs reported in this work were calculated at a reaction time of 15 min to minimize mass transfer limitations.

Electrocatalytic Hydrogenation of Muconic Acid

The electrocatalytic hydrogenation of *cc*MA to AA was carried out using Pd/CF and Pd/CNF@CF as catalysts, over a 360-min reaction time at a constant potential of −0.7 V versus Ag/AgCl. The operational conditions, *cc*MA solution preparation, and calculation method followed the same procedure as described in the previous section.

Acknowledgements

This material is based upon work supported by the National Science Foundation under award nos. 2218070 and 2132200. L.A. and L.Q. were supported by the U.S. Department of Energy (DOE), Office of Basic Energy Sciences, Division of Chemical Sciences, Geosciences, and Biosciences, Catalysis Science program. The Ames Laboratory is operated for the U.S. DOE by Iowa State University under contract no. DE-AC02-07CH11358. The authors thank D. Jing of Iowa State University's Materials Analysis Research Laboratory for his help with the acquisition and analysis of XPS data.

Conflict of Interest

The authors declare no conflict of interest.

Data Availability Statement

The data that support the findings of this study are available from the corresponding author upon reasonable request.

Keywords: electrochemical hydrogenation · electrosynthesis · hierarchical electrodes · muconic acid · surface chemistry

[1] P. De Luna, C. Hahn, D. Higgins, S. A. Jaffer, T. F. Jaramillo, E. H. Sargent, *Science* **2019**, *364*, eaav3506.
[2] B. A. Frontana-Uribe, R. D. Little, J. G. Ibanez, A. Palma, R. Vasquez-Medrano, *Green Chem.* **2010**, *12*, 2099.
[3] G. M. Martins, G. C. Zimmer, S. R. Mendes, N. Ahmed, *Green Chem.* **2020**, *22*, 4849.
[4] C. Liu, Y. Wu, B. Zhao, B. Zhang, *Acc. Chem. Res.* **2023**, *56*, 1872.
[5] B. K. Kundu, Y. Sun, *Chem. Sci.* **2024**, *15*, 16424.
[6] Y. Xu, Z. Mao, R. Qu, J. Wang, J. Yu, X. Luo, M. Shi, X. Mao, J. Ding, B. Liu, *Nat. Water* **2023**, *1*, 95.
[7] P. Moreno-García, M. D. J. Gálvez-Vázquez, T. Prenzel, J. Winter, L. Gálvez-Vázquez, P. Broekmann, S. R. Waldvogel, *Adv. Mater.* **2024**, *36*, 2307461.
[8] D. S. Mallapragada, Y. Dvorkin, M. A. Modestino, D. V. Esposito, W. A. Smith, B.-M. Hodge, M. P. Harold, V. M. Donnelly, A. Nuz, C. Bloomquist, *Joule* **2023**, *7*, 23.
[9] T. Wu, M.-Y. Han, Z. J. Xu, *ACS Nano* **2022**, *16*, 8531.
[10] M. Boudart, G. Djéga-Mariadassou, *Kinetics of Heterogeneous Catalytic Reactions*, Princeton University Press, New Jersey, USA **2014**.
[11] C. Ledesma, J. Yang, D. Chen, A. Holmen, *Acs Catal.* **2014**, *4*, 4527.
[12] E. Antolini, *Appl. Catal. B* **2009**, *88*, 1.
[13] H. Ren, Y. Wang, Y. Yang, X. Tang, Y. Peng, H. Peng, L. Xiao, J. Lu, H. D. Abruna, L. Zhuang, *ACS Catal.* **2017**, *7*, 6485.
[14] H. Huang, X. Guo, C. Zhang, L. Yang, Q. Jiang, H. He, M. A. Amin, W. A. Alshahrani, J. Zhang, X. Xu, *ACS Nano* **2024**, *18*, 10341.
[15] D. Bernsmeier, L. Chuenchom, B. Paul, S. Rümmler, B. Smarsly, R. Kraehnert, *ACS Catal.* **2016**, *6*, 8255.
[16] C. Zhang, P. Liang, X. Yang, Y. Jiang, Y. Bian, C. Chen, X. Zhang, X. Huang, *Biosens. Bioelectron.* **2016**, *81*, 32.
[17] M. N. Dell'Anna, G. Gupta, P. T. Prabhu, T.-H. Chu, L. T. Roling, J.-P. Tessonnier, *Green Chem.* **2023**, *25*, 10387.
[18] D. M. Patel, P. T. Prabhu, G. Gupta, M. N. Dell'Anna, S. Kling, H. T. Nguyen, J.-P. Tessonnier, L. T. Roling, *Green Chem.* **2024**, *26*, 4506.
[19] I. Khalil, G. Quintens, T. Junkers, M. Dusselier, *Green Chem.* **2020**, *22*, 1517.
[20] M. Suastegui, J. E. Matthiesen, J. M. Carraher, N. Hernandez, N. Rodriguez Quiroz, A. Okerlund, E. W. Cochran, Z. Shao, J. P. Tessonnier, *Angew. Chem. Int. Ed.* **2016**, *55*, 2368.
[21] S. Abdolmohammadi, D. Gansebom, S. Goyal, T.-H. Lee, B. Kuehl, M. J. Forrester, F.-Y. Lin, N. Hernández, B. H. Shanks, J.-P. Tessonnier, *Macromolecules* **2021**, *54*, 7910.
[22] P. Carter, P. M. Meyer, T.-H. Lee, D. Dileep, N. L. Chalgren, S. Noreen, M. J. Forrester, B. H. Shanks, J.-P. Tessonnier, E. W. Cochran, *RSC Sustainability* **2024**, *2*, 2968.
[23] L. De Vriendt, I. Khalil, M. V. Hickson, B. Sels, M. Dusselier, *ChemCatChem* **2025**, e00973, https://doi.org/10.1002/cctc.202500973.
[24] J. E. Matthiesen, M. Suástegui, Y. Wu, M. Viswanathan, Y. Qu, M. Cao, N. Rodriguez-Quiroz, A. Okerlund, G. Kraus, D. R. Raman, *ACS Sustainable Chem. Eng.* **2016**, *4*, 7098.
[25] J. E. Matthiesen, J. M. Carraher, M. Vasiliu, D. A. Dixon, J.-P. Tessonnier, *ACS Sustainable Chem. Eng.* **2016**, *4*, 3575.
[26] L. M. Martins, *Homogeneous Oxidation Reactions*, Elsevier, Amsterdam, Netherlands **2025**, pp. 67–82.
[27] M. K. Sikazwe, J. Louw, J. F. Görgens, *Biofuel Res. J.* **2024**, *11*, 2225.
[28] J. Iglesias, I. Martínez-Salazar, P. Maireles-Torres, D. M. Alonso, R. Mariscal, M. L. Granados, *Chem. Soc. Rev.* **2020**, *49*, 5704.
[29] A. Castellan, J. C. J. Bart, S. Cavallaro, *Catal. Today* **1991**, *9*, 237.
[30] J. Rios, J. Lebeau, T. Yang, S. Li, M. D. Lynch, *Green Chem.* **2021**, *23*, 3172.
[31] E. Skoog, J. H. Shin, V. Saez-Jimenez, V. Mapelli, L. Olsson, *Biotechnology Adv.* **2018**, *36*, 2248.
[32] Y. Liu, J. Luo, C. Helleu, M. Behr, H. Ba, T. Romero, A. Hébraud, G. Schlatter, O. Ersen, D. S. Su, *J. Mater. Chem. A* **2017**, *5*, 2151.

[33] E. García-Bordejé, Y. Liu, D. S. Su, C. Pham-Huu, *J. Mater. Chem. A* **2017**, *5*, 22408.
[34] C. Pham-Huu, R. Vieira, B. Louis, A. Carvalho, J. Amadou, T. Dintzer, M. J. Ledoux, *J. Catal.* **2006**, *240*, 194.
[35] M. J. Becker, W. Xia, K. Xie, A. Dittmer, K. Voelskow, T. Turek, M. Muhler, *Carbon* **2013**, *58*, 107.
[36] J.-P. Tessonnier, D. Rosenthal, T. W. Hansen, C. Hess, M. E. Schuster, R. Blume, F. Girgsdies, N. Pfänder, O. Timpe, D. S. Su, *Carbon* **2009**, *47*, 1779.
[37] R. Blume, D. Rosenthal, J. P. Tessonnier, H. Li, A. Knop-Gericke, R. Schlögl, *ChemCatChem* **2015**, *7*, 2871.
[38] D. Pollok, S. R. Waldvogel, *Chem. Sci.* **2020**, *11*, 12386.
[39] J. M. Carraher, T. Pfennig, R. G. Rao, B. H. Shanks, J.-P. Tessonnier, *Green Chem.* **2017**, *19*, 3042.
[40] M. N. Dell'Anna, M. Laureano, H. Bateni, J. E. Matthiesen, L. Zaza, M. P. Zembrzuski, T. J. Paskach, J.-P. Tessonnier, *Green Chem.* **2021**, *23*, 6456.
[41] Y. Zhang, A. A. Tamijani, M. E. Taylor, B. Zhi, C. L. Haynes, S. E. Mason, R. J. Hamers, *J. Am. Chem. Soc.* **2019**, *141*, 8277.
[42] L. Feng, Q. Liu, G. Xu, M. Ge, W. Bi, Y. Huang, J. Zhang, X. Liu, S. Chen, F. Nie, *ACS Catal.* **2025**, *15*, 4394.
[43] M. McGovern, E. Garnett, C. Rice, R. Masel, A. Wieckowski, *J. Power Sources* **2003**, *115*, 35.
[44] Z. Pan, Y. Bi, L. An, *Appl. Energy* **2020**, *258*, 114060.
[45] G.-F. Li, D. Yang, P.-Y. Abel Chuang, *ACS Catal.* **2018**, *8*, 11688.
[46] H. Ba, L. Truong-Phuoc, Y. Liu, C. Duong-Viet, J.-M. Nhut, L. Nguyen-Dinh, P. Granger, C. Pham-Huu, *Carbon* **2016**, *96*, 1060.
[47] M. C. Biesinger, *Appl. Surf. Sci.* **2022**, *597*, 153681.
[48] A. J. Lizarbe, G. H. Major, V. Fernandez, N. Fairley, M. R. Linford, *Surf. Interface Anal.* **2023**, *55*, 651.
[49] D. R. Baer, K. Artyushkova, H. Cohen, C. D. Easton, M. Engelhard, T. R. Gengenbach, G. Greczynski, P. Mack, D. J. Morgan, A. Roberts, *J. Vacuum Sci. Technol. A* **2020**, *38*, 031204.
[50] M. Knauer, M. E. Schuster, D. Su, R. Schlögl, R. Niessner, N. P. Ivleva, *J. Phys. Chem. A* **2009**, *113*, 13871.

Manuscript received: August 15, 2025
Revised manuscript received: September 25, 2025
Version of record online: